Research Square

Preprints are preliminary reports that have not undergone peer review.
They should not be considered conclusive, used to inform clinical practice,
or referenced by the media as validated information.

A Preimage-Based Framework for Whisker Sensing and Robot Localization

Prasanna K. Routray

prasanna.routray97@gmail.com

Indian Institute of Technology Madras

Basak Sakcak

University of Oulu

Steven M. LaValle

University of Oulu

Manivannan M.

Indian Institute of Technology Madras

Research Article

Keywords: Whisker sensor, Touch sensing, Cantilever beam, Preimage, Virtual sensor models, Robot localization

Posted Date: May 27th, 2026

DOI: https://doi.org/10.21203/rs.3.rs-9468985/v1

License: This work is licensed under a Creative Commons Attribution 4.0 International License.
Read Full License

Additional Declarations: No competing interests reported.

A Preimage-Based Framework for Whisker Sensing and Robot Localization

Prasanna K. Routray[1*], Basak Sakcak[2,3†], Steven M. LaValle[2†], Manivannan M.[1†]

[1*]Applied Mechanics and Biomedical Engineering, Indian Institute of Technology Madras, Chennai, 600036, TamilNadu, India.
[2]Faculty of Information Technology and Electrical Engineering, University of Oulu, Oulu, 90570, Oulu, Finland.
[3]Department of Advanced Computing Sciences, Maastricht University, Maastricht, the Netherlands.

*Corresponding author(s). E-mail(s): prasanna.routray97@gmail.com;
Contributing authors: basak.sakcak@oulu.fi; steven.lavalle@oulu.fi; mani@iitm.ac.in;
†These authors contributed equally to this work.

Abstract

Conventional development of robotic whiskers is largely hardware-centric. This paper instead formulates whisker sensing as an observation-modeling problem by deriving a hierarchy of virtual sensor models from large-deflection cantilever beam mechanics. These models serve as mathematical abstractions characterizing the uncertainty induced by the many-to-one nature of a sensor mapping, independent of the physical implementation of the sensors. By leveraging these virtual models, we establish a formal ordering of sensing modalities based on the extent to which they reduce state-uncertainty. We analyze how different whisker sensors encode geometric information by characterizing the preimages they induce, which systematically partition the combined robot-whisker state-space. This theoretical framework is then applied to planar robot self-localization. Global pose is resolved through the recursive intersection of the preimages of observations under a given sensor mapping alongside known incremental motion. To overcome the inherent sensitivity of strict deterministic intersections to real-world noise, we exploit a possibilistic approach that accommodates bounded observation uncertainty, ensuring robust localization. The framework is evaluated through numerical simulations with known ground-truth contact geometry, and through physical experiments validated by a high-precision linear stage. These results demonstrate successful contact estimation and the strategic exploitation of tip-contact transitions to rapidly accelerate the contraction of feasible robot states. Overall, evaluating sensing modalities through state-space partitioning provides a mathematical guideline for purposeful, task-oriented whisker sensor design linked directly to downstream navigation performance.

Keywords: Whisker sensor, Touch sensing, Cantilever beam, Preimage, Virtual sensor models, Robot localization

Nomenclature

L	Total length of the beam or whisker
a	Load position on undeformed beam, from fixed end, $0 \leq a \leq L$
s	arc-length along deformed beam, $0 \leq s \leq L$
s_a	arc-length at load position
$\phi(s)$	Slope of beam, positive clockwise
ϕ_a	Slope at load point ($s = s_a$)
$x(s)$	Horizontal coordinate of deformed beam
$y(s)$	Vertical coordinate of deformed beam
δ_x	Horizontal displacement at tip, $L - x(s)$
δ_y	Vertical displacement at tip, $-y(s)$
$p = (p_x, p_y)$	Cartesian position of contact point in sensor frame
$\mathcal{P}$	Set of contact points in sensor frame
d	distance between (p_x, p_y) and sensor reference frame
F	Magnitude of the point load, applied vertically at $s = s_a$
F_x, F_y	Reaction forces at the fixed end of the beam ($s = 0$)
κ	Beam curvature ($\frac{d\phi}{ds}$)
$M(s)$	Bending moment at arc-length (s)
Y	Young's modulus of the beam material
I	Moment of inertia of the beam's cross-section
$\mathcal{C}$	Configuration space
Q	State space
Z	Observation space
$h^{-1}(z) \subset Q$	Preimage of $z \in Z$ under $h : Q \to Z$
$h : Q \to Z$	Sensor mapping
θ_{add}	Sensor base rotation angle
T	Homogeneous transform
t_x	Linear displacement along x-axis
t_y	Linear displacement along y-axis
$q_r = (q_x, q_y, q_\theta)$	State of the robot
q_s	State of the sensor
$\{x_E, y_E, \phi_E\}$	Position and slope of map boundary
ϕ_{E_i}	Instantaneous slope of the boundary from sensor observation
γ	Angle between beam shape and boundary at contact point
Δ	Triangulation
ϵ	Error in estimation
$\alpha \in [0, 1]$	Whisker deflection parameter
$\sigma_\alpha \in \mathbb{R}^2$	Shape of deflected whisker
$A \subseteq Z$	An interval around the noisy observation z

1 Introduction

Autonomous robotic navigation in visually degraded and confined environments remains a fundamental challenge. Conventional perception modalities, such as cameras and LiDAR, often degrade or fail at close range because of self-occlusion, airborne particulates, and optically challenging reflective or transparent surfaces (Struckmeier et al. (2019); Chen et al. (2022)). Biological systems provide a useful model for addressing this gap in near-field perception: mammals such as rodents and felids rely on whiskers to navigate effectively when visual cues are limited or absent (Mitchinson et al. (2007)). Motivated by this capability, artificial whisker sensors have emerged as a complementary sensing modality for robotics. By providing direct contact-based information about the surrounding environment, they can support perception and interaction in settings where conventional visual sensors are unreliable (Fox et al. (2012); Struckmeier et al. (2019)).

Artificial whiskers function as both tactile and proprioceptive sensors, with observations arising from mechanical interaction with the environment. Unlike remote sensing modalities, whisker signals are generated by the contact-induced deformation of a slender cantilever beam (Kaneko et al. (1998); Huet et al. (2017)). As a result, sensing performance depends strongly on both the physical design of the whisker and the way it is instrumented. Although the underlying beam mechanics remain the same, a single physical interaction can produce several distinct and mathematically meaningful observations, including base bending moment, applied load, contact location, local slope, and deflected shape (Solomon and Hartmann (2011); Huet et al. (2017)). Use of whisker sensors in robotics poses a challenge in the mapping of whisker sensor observation to robot state which is generally non-injective, making individual observations intrinsically ambiguous (Solomon and Hartmann (2010); Lin et al. (2022)). To represent this ambiguity explicitly, we use the preimage of an observation: the set of

robot states consistent with the measured mechanical response (LaValle et al. (2012); Bilevich et al. (2023)).

This article analyzes robot state uncertainty based on whisker sensor observations, providing a fundamental understanding of the sensor that can be easily linked to suitable design for mobile robots. In our formulation, state uncertainty is constrained by sequentially accumulating tactile observations as the robot follows known trajectories. Estimation proceeds by intersecting the preimages (feasible sets) associated with current and past observations. To standardize this process across modalities, we employ a shape-based parameterization that provides a common geometric basis for relating mechanical observations to the environment and the robot pose (Kaneko et al. (1998); Solomon and Hartmann (2010); Huet et al. (2017); Lin et al. (2022)).

The remainder of this article is organized as follows. Section 2 presents the literature review. Section 3 defines the formal problem formulation. Section 4 analyzes ambiguity associated with sensor model through preimages. Section 5 presents filtering strategies. Section 6 reports experimental results, and Section 7 discusses the assumptions and limitations.

2 Literature Review

Robotic whisker systems span diverse design paradigms, ranging from passive arrays to actively driven sensors (Yu et al. (2024); Wang et al. (2023); Prescott et al. (2009)). While these designs employ varied transduction methods—including resistive, magnetic, and optical approaches (Takei et al. (2014); Lepora et al. (2018); Deer and Pounds (2019); Kim et al. (2019))—their primary function remains contact transduction (Kaneko et al. (1998); Kim and Möller (2007); Solomon and Hartmann (2010); Ahn and Kim (2017); Lin et al. (2022); Sofla et al. (2024)). Regardless of the underlying hardware or the physical properties of the sensor (Pearson et al. (2011); Boubenec et al. (2012)), interpreting the sensor observations fundamentally constitutes an inverse mechanics problem aimed at estimating the deflected shape of the whisker and the specific point of contact.

2.1 Mechanics and Identifiability

To mathematically represent this contact-induced deformation, current methods typically model the whisker as a cantilever beam governed by Euler–Bernoulli theory or Cosserat-rod formulations (Gazzola et al. (2018)). The central analytical bottleneck in this process is inverse identifiability: the ability to map sensor observations, such as bending moments or base reaction forces, back to a unique contact geometry. While analytical models define the underlying mechanics, research leveraging learning-based regression (Emnett et al. (2018)) and analytical filtering (Kaneko et al. (1998); Kim and Möller (2006); Sofla et al. (2024); Lin et al. (2022)) demonstrates that while specific signal triplets can uniquely determine 3D contact, other observation combinations remain intrinsically ambiguous (Huet et al. (2017); Starostin et al. (2023); Huet et al. (2022)). Furthermore, factors such as intrinsic curvature and taper strongly condition the sensor observation (Birdwell et al. (2007); Solomon and Hartmann (2011)), requiring meticulous calibration to prevent systemic bias (Quist and Hartmann (2012)).

2.2 State Estimation and Ambiguity

Even with local contact recovery, an isolated whisker observation rarely determines a unique robot state. Because the same mechanical observation can arise from different robot states, contact-driven observations are inherently ambiguous—a challenge recognized in earlier active-probing work (Kaneko et al. (1998); Pearson et al. (2007)) and often addressed through probabilistic methods such as Tactile SLAM (Fox et al. (2012)), Whisker-RatSLAM, and visuo-tactile fusion (Struckmeier et al. (2019)).

In this work, we bridge the gap between ambiguous mechanical signals and global localization by shifting the interpretation of this inverse problem to the lens of robot state uncertainty. We formalize this by modeling the whisker as a virtual sensor (LaValle et al. (2012); Tiwari et al. (2022)), where each observation modality defines a mapping from robot state to sensor observation. Because this mapping is generally non-injective, a single observation induces a *preimage*: the set of all feasible robot state set consistent with the recorded data. Global localization is then

approached by recursively intersecting these feasible robot state sets over time (Bilevich et al. (2023); Jaulin (2009); Guyonneau et al. (2014)). This geometric abstraction characterizes the sensor through feasible sets rather than raw signals, providing a common representation across sensing modalities and enabling a formal analysis of how different observations induce ambiguity within a known environment.

3 Problem Formulation

We consider the planar self-localization of a mobile robot equipped with a single flexible whisker sensor. The robot state q is expressed by the triple, that is, $q = (x, y, \theta)$, in which $(x, y) \in E$ is the robot position in a known environment $E \subseteq \mathbb{R}^2$ and $\theta \in S^1$ is the orientation with respect to a global reference frame. We assume that E is compact and the boundary ∂E is smooth. We further assume that the set of robot positions E is static (it is not time dependent) and the environment is rigid so that it does not change under contact. In the following, will use $q_t = (x_t, y_t, \theta_t)$ to denote the robot state at time t. The robot state space is denoted by $Q := E \times S^1$.

The robot motion is given by a state transition equation as $q_{t+1} = f(q_t, u_t)$, in which $u_t \in U$ is the action at time t. The target of this work, whisker sensors, can yield a different observation while the robot is at the same state depending on the whisker shape. To account for this, we introduce an augmented state space Q_{aug} which encompasses both the robot state q and the whisker state α, such that $(q, \alpha) \in Q_{\text{aug}}$. The whisker shape is parametrized by the whisker state α such that $\sigma_\alpha : [0, 1] \to \mathbb{R}^2$ gives the curve corresponding to the whisker with respect to a robot-fixed reference frame.

Considering this augmented state space Q_{aug}, we define a sensor mapping $h : Q_{\text{aug}} \to Z$ which maps the robot state q and the whisker shape α to a unique observation z, that is $z := h(q, \alpha)$. However, this mapping is oftentimes not bijective meaning that the preimage of z under h is not necessarily unique.

The objective is to estimate the robot state at time t, that is, determine an estimate of $q_t = (x_t, y_t, \theta_t) \in Q$, for all $t = 0, 1, \ldots$, within a known rigid two-dimensional environment given the contact observations z_t, the robot motion and sensing models described by the functions f and h, and the applied control u_{t-1}.

Assumptions and Scope

The formulation considered here is restricted to static, rigid environments; compliant obstacles are outside the scope of the present study. Physical interaction is modeled as quasi-static, assuming the beam deformation occurs slowly enough that internal elastic forces remain in constant equilibrium with external contact forces, allowing inertial and damping effects to be neglected. Dynamic friction and slip effects, which may aid contour extraction in other settings (Solomon and Hartmann (2010)), are not modeled. In addition, robot motion between observations is treated as known through the input u_t (e.g., through calibrated odometry), so that the analysis can focus on sensing ambiguity rather than uncertainty in the motion model.

4 Whisker Sensor

This section establishes the relation between the physical mechanics of whisker sensors and the resulting uncertainty in the robot state. By modeling the whisker as a flexible cantilever beam, we derive a taxonomy of sensor models that map mechanical interactions to specific observations. We then utilize the notion of preimages to analyze the partitioning of the state space induced by different sensors. This analysis provides a fundamental understanding of the relationship between sensor design and spatial ambiguity, demonstrating how specific mechanical measurements constrain the set of possible robot states within a known environment. These geometric foundations serve as the basis for the fusion and filtering strategies developed in the remainder of this work.

4.1 Whisker Mechanics

We see a whisker sensor similar to a cantilever beam. Therefore, the mechanical response of the whisker sensor is modeled using Euler–Bernoulli beam theory, which describes the relationship between environmental contact loads and the resulting sensor observations. Contact with the environment induces a lateral load on the cantilever beam, which in turn generates reaction forces and bending moments at the fixed base.

Depending on the load magnitude, the beam undergoes either small-angle deflections, typically characterized by tip displacements below 10% of the beam length L, or large-angle deformations. As illustrated in Fig. 1a, the sensor is modeled as a cantilever capable of large-angle deflection. The deflected beam shape is parameterized by the coordinates $x(s)$ and $y(s)$ as functions of arc length s. The local slope, denoted by $\phi(s)$, increases from zero at the base to a maximum value ϕ_a at the point of load application, producing tip displacements δ_x and δ_y. Under large-angle deformation, the horizontal displacement δ_x becomes geometrically significant (Fig. 1b). The beam mechanics are governed by the local curvature $\kappa(s)$, which relates the bending moment $M(s)$ to the flexural rigidity YI, where Y is Young's modulus and I is the area moment of inertia:

$$\kappa(s) = \frac{d\phi(s)}{ds} = \frac{M(s)}{YI}.$$

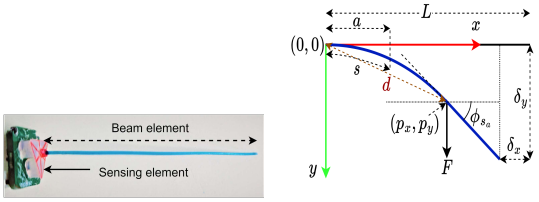
For large deflections, the mapping from an applied contact load to the deflected whisker shape $(x(s), y(s), \phi(s))$ is governed by the nonlinear planar elastica equations and is evaluated numerically (Appendix A).

4.2 Sensor models

A quasi-static contact event yields an observation vector z_t, which can also be a scalar, comprising specific mechanical or geometric quantities extracted from the deflected whisker. The observation depends on the specific hardware architecture used. While certain components (e.g., base moment M or contact arc-length s_a) may be directly measured by physical transducers, others function as virtual quantities inferred analytically via the established beam mechanics. To systematically evaluate how specific observation modalities mitigate spatial ambiguity, we define a taxonomy of *whisker sensor models*. Each model represents a distinct, deterministic mapping from the augmented robot state space Q_{aug} to an appropriate observation space Z.

Binary Contact Detector

The binary contact detector represents the simplest form of whisker feedback, signaling whether a collision has occurred between the sensor and the environment.



(a) (b)

Fig. 1: (a) Physical whisker sensor mounted at a fixed base. (b) Whisker sensor modeled as a planar clamped-free cantilever whose centerline deforms upon contact with the environment.

Model 1 (**Binary Contact Detector**). *This sensor provides a binary observation based on the contact state of the whisker beam:*

$$h_{bs}(q, \alpha) = \begin{cases} 1 & \text{if } W(q, \alpha) \cap \partial E \neq \emptyset \\ 0 & \text{otherwise} \end{cases} \tag{1}$$

where $W(q, \alpha) \subset E$ is the set of points occupied by the whisker in the environment for a given robot state q and whisker shape α.

Contact is defined by a non-empty intersection between the whisker and the environmental boundary ∂E. For a contact observation $z = 1$, the feasible robot state set is the collection of all robot states q that satisfy this intersection condition.

Applied Load

The applied load is denoted by F and acts laterally at arc-length s_a. Together with (s_a, ϕ_a), the load determines the contact point $p = (x(s_a), y(s_a))$ and the corresponding centerline shape via the large-angle beam equations (see Appendix A).

Model 2 (**Load Sensor**). *This sensor measures the frictionless normal force F acting laterally at a single point along the whisker beam:*

$$h_{ls}(q, \alpha) = F, \tag{2}$$

where $F \in [-F_{\max}, F_{\max}]$. The maximum magnitude $F_{\max}$ represents the limit beyond which plastic deformation of the beam occurs. A negative value indicates force applied along the negative y_s-axis (see Fig. 1b).

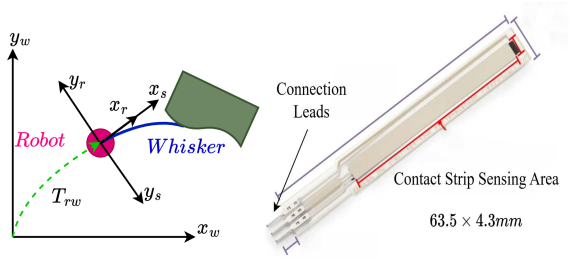
Contact Location Along the Whisker

The contact location is parameterized by the arc-length $s_a \in [0, L]$, measured from the base to the point of contact along the whisker centerline. This partitions the whisker into a loaded segment $[0, s_a]$ and an unloaded segment $(s_a, L]$ with constant slope ϕ_a (Appendix A).

Model 3 (**Contact Strip Sensor**). *This sensor reports the region of the whisker that is in contact with the environment. Let the whisker be discretized into intervals* $\mathcal{J} = \{J_i\}_{i=1}^{N}$ *such that* $\bigcup_{i=1}^{N} J_i = [0, L]$, *with* $J_i = [s_{i-1}, s_i]$. *Assuming single-point contact, the sensor returns the interval containing the contact arc-length* s_a*:*

$$h_{css}(q, \alpha) = J_a, \qquad s_a \in J_a. \tag{3}$$

A typical realization is shown in Fig. 2b.



(a) (b)

Fig. 2: Reference frames for the robot T_{rw} and whisker sensor in world reference frame: (a) Whisker sensor (blue) mounted on a robot and making a contact with the environment. (b) A commercial contact strip sensor available from TekScan™ can act like a whisker sensor.

End-Slope at Contact

The tangent angle at contact is $\phi_a = \phi(s_a)$. It determines the orientation of the unloaded segment and becomes crucial in the large-angle relations used to reconstruct the loaded segment and infer the contact point p when (F, s_a, ϕ_a) are available (see Fig. 1b).

Model 4 (**End-slope sensor**). *This sensor measures the maximum slope of the whisker beam, denoted by* ϕ_a*, under a transverse normal load:*

$$h_{es}(q, \alpha) = \phi_a, \tag{4}$$

where $\phi_a \in \left[-\frac{\pi}{2}, \frac{\pi}{2}\right]$ *is the slope at contact point.*

Base Bending Moment

Base observations—particularly the bending moment $M(0)$—are widely used because embedding distributed sensors along a slender whisker is often impractical.

Model 5 (**Bending moment sensor**). *This sensor measures the bending moment at the whisker base:*

$$h_{bms}(q, \alpha) = M(0), \tag{5}$$

where $M(0) \in [-M_{\max}, M_{\max}]$. *A negative (clockwise) moment indicates loading along the* y_s*-axis. If the magnitude exceeds* $M_{\max}$*, the beam may not return to its original shape.*

For flexible whiskers, small-angle approximation limits the modeling accuracy; in this work we use a large-angle beam model (Appendix A) to define virtual sensor mappings and to reconstruct $(\phi_{a,t}, \hat{\sigma}_t)$ from z_t. In simulation, we also leverage the efficient numerical implementation of large-angle 2D deflection developed by Quist and Hartmann (2012) to circumvent the repeated evaluation of elliptic-integral expressions when generating reconstructed beam shapes.

4.3 Partial Observability

The augmented state space Q_{aug} is defined to encompass both the robot state q and the whisker shape α, such that $(q, \alpha) \in Q_{\text{aug}}$. For a given virtual sensor mapping $h : Q_{\text{aug}} \to \mathcal{Z}$, the preimage of z under h is defined as

$$h^{-1}(z) = \{(q, \alpha) \in Q_{\text{aug}} \mid h(q, \alpha) = z\}. \tag{6}$$

The collection of preimages corresponding to all realizable observations under h forms a partition of Q_{aug}, denoted by

$$\Pi(h) = \{\, h^{-1}(z) \mid z \in h(Q_{\text{aug}}) \,\}. \tag{7}$$

Its elements are equivalence classes of augmented states that are indistinguishable under the chosen observation. Formally, two augmented states (q, α) and (q', α') are indistinguishable whenever $h(q, \alpha) = h(q', \alpha')$. This subsection characterizes the robot state partial-observability patterns for the virtual models introduced previously.

Dummy Sensor

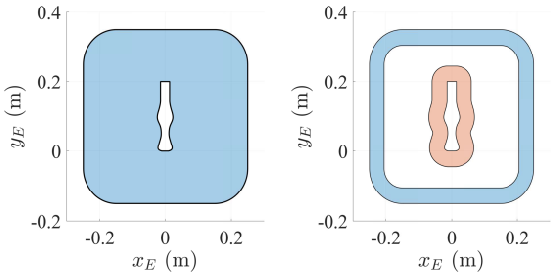
A dummy whisker sensor yields a null observation ($z = \emptyset$), which provides no information regarding the state. Because this observation does not distinguish between any specific whisker shapes or contact locations, the preimage of the null observation coincides with the entire free space of the known map. For instance, in the environment depicted in Fig. 3a, the set of feasible robot states is represented by the entire shaded region. Mathematically, the preimage of the null observation spans the full augmented state space:

$$h^{-1}_{dummy}(\emptyset) = Q_{\text{aug}}, \tag{8}$$

indicating that every state in Q_{aug} is consistent with the observation, resulting in complete uncertainty regarding the robot state and beam shape.

Bump Sensor

Under this modality, a contact observation $z = 1$ indicates that the augmented state (q, α) is consistent with the sensor being in close proximity to a boundary. For a whisker enclosed within a disk of radius r, the resulting preimage $h^{-1}_{bs}(1)$ corresponds to the Minkowski offset of the environmental boundary by radius r (Peternell and Steiner (2007)) (see Fig. 3b). This mapping partitions Q_{aug} by localizing the robot to the boundary neighborhood and excluding all states outside this offset. Consequently, the bump sensor preimage constitutes a proper subset of the dummy sensor's preimage, representing a fundamental reduction in spatial uncertainty. While treated here as a binary detector, the physical whisker provides richer mechanical data, allowing for the even more refined preimages developed in subsequent models.



(a) (b)

Fig. 3: The environment where the robot resides and the corresponding preimage of $z \in \mathcal{Z}$: (a) A map featuring straight, concave, convex, and symmetric boundary sections. The shaded region represents the preimage of a null observation. (b) A single bump observation yields a preimage localized to the shaded region, as the sensor model determines the width of the strip.

Contact Strip Sensor

With a whisker sensor that measures only the arc length s_a along the whisker at which contact occurs, the preimage identifies the states where a map or obstacle boundary is within reach at most s_a units away. Geometrically, this preimage corresponds to a Minkowski offset of the boundary whose width depends on s_a (Fig. 3b), rather than a fixed-radius offset as in the binary bump sensor model. An arc-length observation is approximated by an interval J_a such that $s_a \in J_a$, and the corresponding preimage is defined accordingly for $z = s_a$.

In a known map, this observation partitions Q_{aug} by isolating a strip-like family of feasible robot states q whose distance from the boundary is determined by s_a and bounded by L. Simultaneously, it partitions the state space α into a set of all deflected shapes consistent with a contact at s_a. As illustrated in Fig. 4a, because the sensor does not distinguish between different whisker deflections that share the same contact arc-length, the preimage contains a multiplicity of shapes for each contact point. This partition is only further refined by the practical bending limits inherent to the sensor mechanics.

Load Sensor

A load sensor measures a contact force $F \in [-F_{\max}, F_{\max}]$, which identifies a specific family of admissible whisker shapes for a given arc

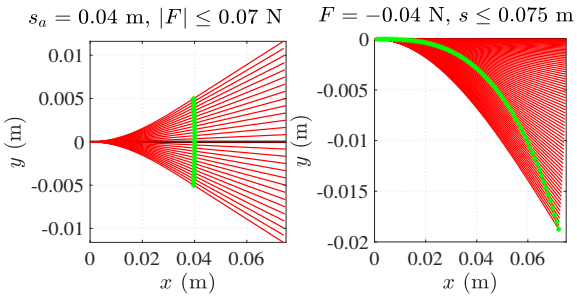


Fig. 4: Possible whisker sensor shapes with practical bending limits. The green curve represents the set of possible contact locations, while the red curves indicate the potential whisker shapes for each contact point: (a) Contact strip sensor, (b) Load sensor.

length s_a. Compared to the preimage of an arc-length-only observation, knowledge of the applied load identifies a smaller subset of feasible whisker shapes and, consequently, a more refined set of robot states. Intuitively, larger load magnitudes correspond to increased whisker bending (see Fig. 4b), yielding a preimage characterized by a narrower strip of robot states relative to the map boundaries.

More formally, for a given load F and arc length $s_a \in [0, L]$, the corresponding end-slope ϕ_a must satisfy:

$$\sqrt{F} = \sqrt{\frac{YI}{2s_a^2}} \int_0^{\phi_a} \frac{1}{\sqrt{\sin\phi_a - \sin\phi}}, d\phi, \qquad \phi \leq \phi_a. \tag{9}$$

Each valid pair (s_a, ϕ_a) determines a unique whisker shape (see Section 4.1 and Appendix A), from which a corresponding contact point $(p_x, p_y) = (x(s_a), y(s_a))$ is extracted. In this context, the observation $z = F$ partitions Q_{aug} by excluding all deflected shapes and robot states that do not satisfy the large-angle beam mechanics for the measured load, defining the preimage accordingly. Thus, an observation that includes the load at the contact point partitions Q_{aug} more finely than simple arc-length sensing. This result is due to the preimage of the load sensor isolating a specific subset of whisker shapes within the broader family of shapes associated with a given s_a. Consequently, the load observation distinguishes between states that were previously indistinguishable, leading to a more refined preimage.

End-slope Sensor

Given an end-slope observation ϕ_a, the admissible parameter pairs (s_a, F) are those that satisfy Eq.(13) for $F \in [-F_{\max}, F_{\max}]$ and $s_a \in [0, L]$. Each admissible pair (see Fig. 5a) defines a specific candidate beam shape and a corresponding contact point, and the corresponding preimage is defined accordingly for $z = \phi_a$.

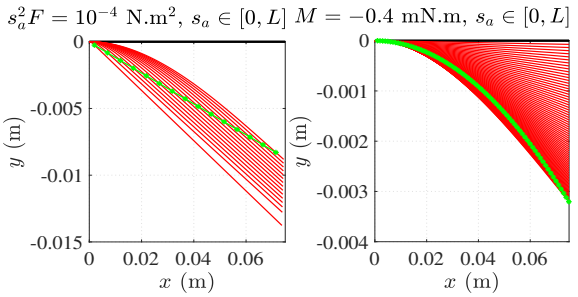


Fig. 5: Set of possible contact points (green) where the whisker sensor may interact with the obstacle. Corresponding flexible beam shapes for a discrete set of sensor observations (red): (a) End-slope sensor. (b) Base bending moment sensor in small-angle deflection case.

The preimage associated with measuring only the end-slope ϕ_a is comparable to that of a load-only sensor (F). This is because both end-slope and load are signed quantities, which partitions the family of admissible beam shapes by a specific bending direction. In contrast, the arc length s_a is strictly nonnegative; when observed in isolation, it lacks directional information, yielding a larger preimage and uncertainty. Geometrically, the end-slope observation ϕ_a induces a boundary-adjacent preimage similar in extent to that produced by a load observation, as illustrated in Fig. 3b.

Bending Moment Sensor

For a bending moment sensor with observation model $h_{bms}(q, \alpha) = M(0)$, the resulting partition of the state space depends on the deflection regime of the whisker. In the small-angle regime, the base moment satisfies

$$M(0) = F s_a, \tag{10}$$

whereas in the large-angle regime, the base moment follows the full beam model,

$$M(0) = Fx(s_a) = \sqrt{\frac{FYI}{2}} \int_0^{\phi_a} \frac{\cos\phi}{\sqrt{\sin\phi_a - \sin\phi}}\, d\phi. \tag{11}$$

In both regimes, multiple parameter tuples (F, s_a, ϕ_a)—and therefore multiple whisker shapes α—consistent with a single observation $M(0)$, yielding the corresponding preimage for $z = M(0)$. In the small-angle case, the geometric interpretation of the bending moment observation yields a preimage comparable to that of a load or end-slope sensor (see Fig. 3b for possible shapes), representing a similarly refined partition of Q_{aug}. In contrast, in the large-angle case, the nonlinear coupling between F, s_a, and ϕ_a corresponds to a broader family of beam shapes consistent with the observation. This results in a strictly larger preimage, which equates to a coarser partition of the augmented state space.

4.4 Spatial Sensor Fusion

When multiple observation components are available from the same whisker sensor body, their joint observation partitions Q_{aug} through the intersection of the corresponding preimages. Let $(z^{(1)}, \ldots, z^{(k)}) \in$ be a k-dimensional observation vector corresponding to the observations coming from k different sensors given by the sensor mappings $h_1 : Q_{\text{aug}} \to Z_1, \ldots, h_k : Q_{\text{aug}} \to Z_k$, in which Z_i is $i = 1, \ldots, k$ denotes the set of possible observations for sensor i. Given the observations coming from different sensors we can define a general triangulation principle (see, LaValle et al. (2012)) which determines the set of states that are consistent with the given observations, similar to the preimage of an observation under a sensor mapping. The triangulation of the observations, denoted by $\triangle(z_1, \ldots, z_k)$ is obtained as the intersection of the individual preimages, that is,

$$\triangle(z_1, \ldots, z_k) := \bigcap_{i=1,\ldots,k} h_i^{-1}(z_i).$$

For example, the preimage resulting from a combined load observation F and a contact-strip observation s_a is defined as:

$$\triangle(F, s_a) = h_{ls}^{-1}(F) \cap h_{css}^{-1}(s_a). \tag{12}$$

In the following, we introduce three new sensor models that are obtained by composing the models introduced in Section 4.2. The preimages corresponding to these virtual sensors are then determined using the general triangulation principle given in Eq. Eq.(12). The following proposition establishes an equivalence relationship across different sensor combinations.

Load and Contact Strip Sensor

Consider a sensor that simultaneously measures both the contact force F and the contact arc length s_a. Under the cantilever beam model, this paired observation partitions the augmented state space more finely by identifying a specific deflected shape and end-slope ϕ_a, which determines the contact point within the sensor reference frame.

Specifically, the relationship between the end-slope ϕ_a and the observation pair (F, s_a) is governed by:

$$s_a\sqrt{F} = \sqrt{\frac{YI}{2}} \int_0^{\phi_a} \frac{1}{\sqrt{\sin\phi_a - \sin\phi}}\, d\phi, \tag{13}$$

in conjunction with the standard cantilever beam kinematics (see Subsection 4.1 and Appendix A).

Fig. 6 and equation Eq.(12) demonstrate that the intersection of the feasible pose sets—induced by the individual components of the same whisker body—results in a significantly more localized preimage. Furthermore, given the observations defined by the pairs $\{F, s_a\}$, $\{s_a, \phi_a\}$, and $\{F, \phi_a\}$ are informationally equivalent. Accordingly, each robot state induces an identical partition of the augmented state space $\mathcal{Q}_{\text{aug}}$. This is demonstrated in the following Proposition.

Proposition 1 *Consider the cantilever mechanics described in Appendix A). Given any two quantities from the set $\{F, s_a, \phi_a\}$, the third is uniquely determined via the relation established in (A2). Consequently, the observations (Type A) $\{F, s_a\}$, (Type B) $\{F, \phi_a\}$, and (Type C) $\{s_a, \phi_a\}$ are informationally equivalent, as each uniquely resolves the contact point (p_x, p_y) and the complete deflected shape $\hat{\sigma}_t$ of the whisker.*

Proof For the deflection regime $\phi_a \in (0, \pi/2)$, the right-hand side of (A2) is continuous, positive, and

strictly monotonic in ϕ_a. This monotonicity establishes a well-posed mapping among F, s_a, and ϕ_a:

- **Given F and s_a (Type A):** (A2) becomes a scalar nonlinear equation in ϕ_a. Due to the strict monotonicity of the integral, a unique solution for ϕ_a exists.
- **Given F and ϕ_a (Type B):** The application arc-length s_a is determined directly by explicit quadrature of the relation in (A2).
- **Given s_a and ϕ_a (Type C):** The force F is recovered by rearranging (A2) into the following form:

$$F = \frac{YI}{2}\left(\frac{1}{s_a}\int_0^{\phi_a}\frac{d\phi}{\sqrt{\sin\phi_a - \sin\phi}}\right)^{-2}.$$

In all three cases, the complete state triad $\{F, s_a, \phi_a\}$ is resolved. This allows for the deterministic reconstruction of the deflected beam shape $x(s), y(s)$ through (A1) and (A3), and the base moment $M(0) = Fx(s_a)$. Thus, each pair of inputs is sufficient to uniquely define the whisker shape and the resulting pose preimage. □

This equivalence ensures that the observation of any two parameters within the set $\{F, s_a, \phi_a\}$ uniquely resolves the same set of whisker shapes $\hat{\sigma}_t$ and contact coordinates (p_x, p_y) via the underlying cantilever mechanics. Thus, the resulting pose preimage is invariant to the specific choice of the observation pair used to characterize the large-deflection state.

Bending Moment and Contact Strip Sensor

This sensing modality represents a desirable augmentation to the set of physically realizable whisker-based sensors. The bending moment observation can be interpreted through the underlying beam mechanics (Eqs. Eq.(10)–Eq.(11)) to define a precise preimage in the augmented state space.

In the small-angle regime, a sensor measuring both bending moment and contact location yields a preimage comparable to that of a sensor observing load and arc length, representing a similarly refined partition of Q_{aug}. However, in the large-angle regime, the resulting preimage remains strictly larger than that of the load and arc-length combination. This coarser partition is due to the multiplicity of robot states remaining consistent with the moment data under large deflections.

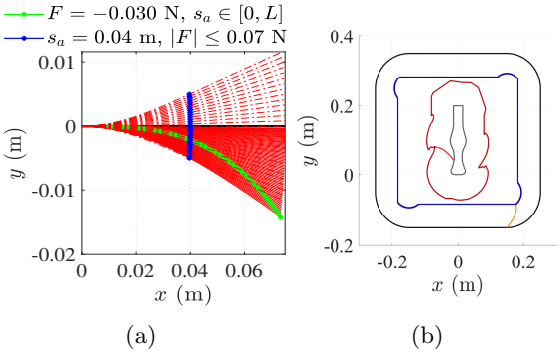


Fig. 6: Intersection of preimages from two observation components in a single whisker sensor. (a) Possible whisker shapes (red) in the sensor reference frame for $s \in [0, L]$ when F is observed, versus shapes for $F \in [-F_{\max}, F_{\max}]$ when s_a is observed. The feasible contact-point sets induced by the load observation (green) and the contact-strip observation (blue) intersect to reduce contact ambiguity. (b) The reduced uncertainty in the contact point yields a refined preimage, indicating lower robot-state uncertainty compared to the single-component case shown in Fig. 3b.

Corollary 1 *In the small-angle (linear) regime, the base bending moment $M(0) \approx Fs_a$ provides an additional mapping that allows the indirect determination of the applied force F from the base moment and contact arc-length s_a. In this regime, the observation pair $\{M(0), s_a\}$ is sufficient to uniquely define the whisker shape and the resulting feasible robot state set. This property holds asymptotically and does not extend to the general nonlinear large-deflection case.*

Addition of Orientation Sensor

Incorporating an orientation sensor (e.g., a compass or IMU) that provides the sensor or robot orientation in the map reference frame fundamentally reduces the resulting preimage. Such orientation information complements the contact-based observations by partitioning the state space according to the measured heading, thereby excluding angular poses inconsistent with the observation. Consequently, the intersection of this orientation preimage with the contact-sensor preimages results in a significantly finer overall partition of Q_{aug}.

4.5 Comparison of Sensor Models

Using the partition $\Pi(h)$ defined in Eq. (7), we now establish a hierarchy of sensor models through

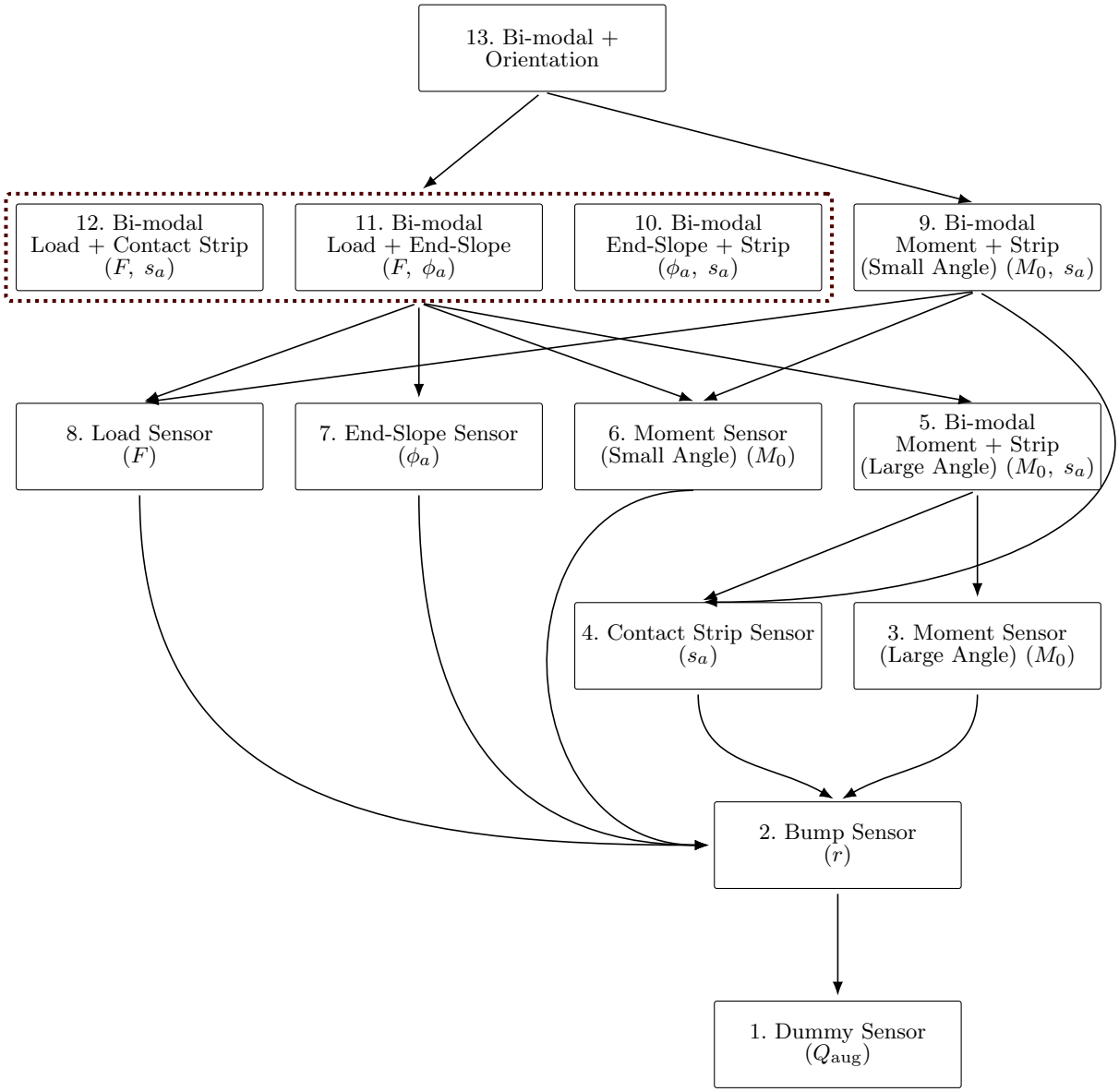


Fig. 7: Hierarchy of sensor models from Section 4.2 and Bi-modal sensor models, organized by the refinement of their induced preimages. Moving upward through the tree, the addition of observation components yields a finer partition of the augmented state space Q_{aug} under the cantilever beam mechanics. Conversely, moving downward corresponds to progressively coarser partitions. Because the preimages of higher-level models are nested subsets of those below them, higher-level models can recover the coarser observation model by omitting components, thereby recovering the coarser preimage associated with the lower-level model.

partition refinement on Q_{aug}. In particular, a sensor model is considered more informative when it induces a finer partition, i.e., smaller equivalence classes of augmented states consistent with a given observation. At the base of this hierarchy lies the **Dummy Sensor**, which induces the coarsest partition, with all augmented states remaining indistinguishable. The **Bump Sensor** yields a finer partition by restricting the admissible states to those consistent with contact near the environment boundary. The **Contact Strip Sensor** provides a further refinement by narrowing the equivalence classes according to the observed contact arc length. Additional physical observables,

such as **Load** or **Moment**, refine the partition further by imposing stronger constraints on the whisker configurations compatible with the observation. The finest partition in this hierarchy is induced by a **Bi-modal sensor**, which jointly observes load and contact arc length.

Furthermore, Proposition 1 implies that the **Bi-modal sensor** models (Models 10–12) are equivalent, in the sense that they induce the same partition $\Pi(h)$ of Q_{aug}. Model 9, corresponding to the small-angle deflection regime, induces the same partition only under the assumptions stated in Corollary 1. When an **Orientation Sensor** is combined with any of the bi-modal sensing models, the induced partition becomes strictly finer than that of each individual model and Bi-modal sensor models, since the additional observation further subdivides the corresponding equivalence classes. Equivalently, the intersection of the associated preimages reduces the residual ambiguity in the augmented state and enables faster resolution of the robot state within a known map. The resulting hierarchy of sensor models can therefore be expressed in terms of partition refinement. Here, $\Pi_1 \preceq \Pi_2$ denotes that Π_2 is a refinement of Π_1, meaning that every set in Π_2 is contained as a subset in some set in Π_1. Thus, Π_1 is coarser and Π_2 is finer as partitions of Q_{aug}. The hierarchy can then be written as

$$\begin{aligned}\Pi(h_{dummy}) &\preceq \Pi(h_{bs}) \preceq \Pi(h_{css}) \preceq \Pi(h_{bms}(\text{LA})) \\ &\preceq \begin{cases} \Pi(h_{ls}) \\ \Pi(h_{bms}(\text{SA})) \\ \Pi(h_{es}) \end{cases} \preceq \Pi(h_{\text{bi-modal}}) \\ &\preceq \Pi(h_{\text{bi-modal+orientation}})\end{aligned} \tag{14}$$

This hierarchy (Fig. 7) follows from the refinement relations among the induced partitions $\Pi(h)$. A higher-level sensor model induces a finer partition than a lower-level one, and can therefore simulate it by neglecting observational detail. Conversely, augmenting a lower-level model with additional sensing modalities yields a finer partition by further subdividing the associated equivalence classes. In particular, Models 10–12 induce partitions that are sufficiently fine to uniquely determine the contact location within the whisker reference frame during valid interactions.

Although Bi-modal sensor models 10–12 can uniquely provide the contact point and beam shape, similar contact localization may also be achieved using lower-level models through temporal filtering. Because accurate contact point and beam shape estimation is critical for downstream tasks such as localization, the following section introduces temporal filtering strategies for robust contact point estimation using either multi-modal sensor fusion or sequential observations, followed by robot localization.

5 Filtering Strategy Towards Localization

In the preceding section, we established a hierarchy of virtual whisker sensor models based on the progressive refinement of their induced partitions in the augmented state space Q_{aug}. Higher-level models in the hierarchy can uniquely determine the contact location, whereas lower-level models induce coarser partitions that admit multiple feasible contact locations and whisker deflection configurations σ_α.

To resolve this ambiguity and leverage these sensor models for navigation, this section introduces a comprehensive framework for set-based robot localization. First, we present filtering strategies that utilize multi-modal fusion and temporal intersection to precisely estimate the contact point and isolate the true whisker shape. Next, we detail a boundary alignment procedure that registers this refined contact geometry against a known environment map to compute the resulting preimage of the robot state. Finally, we integrate a kinematic motion model and a bounded-error state estimation formulation, demonstrating how the iterative forward projection and temporal intersection of these pose preimages enable robust localization.

Each observation initially induces a set of feasible contact points along the whisker. Reducing the multiplicity of these contact points directly refines the feasible set of robot states. We can perform this refinement in two complementary ways: (i) by intersecting preimages induced by multiple observation components within the same whisker sensor body (intra-sensor fusion), and (ii) by temporally intersecting feasible sets inferred at successive time steps. The latter exploits the fact

that, during short incremental motions, the contact remains on the same obstacle boundary and the whisker deflection varies continuously.

5.1 Contact Points Estimation via Filtering

To mathematically validate this filtering strategy, we first establish the topological properties of the feasible contact-point sets induced by the virtual sensor models. A single observation from a lower-tier model does not a contact point; rather, it defines an infinite continuum of possible contact points. However, because this locus is strictly governed by the continuous kinematics of the cantilever beam, it forms a well-behaved, unbroken curve in the sensor frame. The following propositions formalize this physical reality, proving that these feasible sets are compact and connected, which guarantees that intersection operations will reliably isolate the true contact point without fracturing into disjoint hypotheses.

Proposition 2 *Let $\mathcal{P} \subset \mathbb{R}^2$ denote the set of contact points inferred from a virtual whisker sensor model. Let $x(s)$ and $y(s)$ denote the continuous functions representing the horizontal and vertical coordinates of the beam shape, parameterized by arc-length $s \in [0, L]$. Then the set*

$$\mathcal{P} = \{(x(s), y(s)) \mid s \in [0, L]\} \tag{15}$$

is compact and connected; that is, $\mathcal{P}$ is bounded and connected.

Proof The interval $[0, L] \subset \mathbb{R}$ is closed and bounded, and hence compact and connected. The mapping $s \to (x(s), y(s))$ is continuous from $[0, L]$ into $\mathbb{R}^2$. The continuous image of a compact and connected set is compact and connected. Thus, $\mathcal{P} \subset \mathbb{R}^2$ is both bounded and connected. □

Proposition 3 *Let $\mathcal{P}_1$ and $\mathcal{P}_2$ be two sets of deflected contact points in $\mathbb{R}^2$, defined as*

$$\mathcal{P}_i = \{(x_i(s), y_i(s)) \mid s \in [0, L]\},$$

where $x_i(s)$ and $y_i(s)$ are continuous functions over the compact interval $[0, L]$. Then, the intersection set

$$\mathcal{P}_C := \mathcal{P}_1 \cap \mathcal{P}_2$$

is compact and connected whenever nonempty. In degenerate cases (singleton or empty), the result holds trivially.

Proof Each $\mathcal{P}_i$ is the image of a continuous function from a compact and connected interval $[0, L] \subset \mathbb{R}$, and therefore $\mathcal{P}_1, \mathcal{P}_2 \subset \mathbb{R}^2$ are compact and connected. While the intersection of connected sets need not be connected in general, in this context both sets represent smooth traces of beam deflection generated by physically consistent and continuous models. Any nonempty intersection $\mathcal{P}_C$ arises from a continuous overlap between these arc-like traces, forming a connected segment or region in $\mathbb{R}^2$.

Since the intersection of compact sets is compact, $\mathcal{P}_C$ is bounded and closed. Thus, $\mathcal{P}_C$ is connected and bounded whenever nonempty. If $\mathcal{P}_C$ is a singleton or the empty set, the result is vacuously true. □

The topological guarantees provided by these propositions are the mathematical engine of the filtering architecture. Because the feasible sets form continuous curves rather than scattered infinite points, intersecting them—whether through the multimodal fusion discussed in Section 4.4 or via temporal filtering—collapses this continuum down to a uniquely isolated contact point. Furthermore, this formalization naturally accommodates the physical edge case of tip contact: if the intersection of these continuous sets is empty, yet the sensor observation remains above a predefined activation threshold, it strictly indicates that the contact has localized to the whisker tip. Consequently, these geometric intersections reliably extract the exact contact point, effectively replicating the capabilities of higher-tier sensors and enabling a precise partition of the augmented state space for robot localization.

5.2 Contact Point Estimation Validation

Leveraging the physical principle that the contact point on an obstacle boundary remains stationary during small, friction-dominant incremental base motions, previous literature has derived closed-form analytical solutions to estimate the contact distance. For instance, under linear base motion t_y and small-angle assumptions, the contact distance d along the whisker can be estimated via:

$$d = \sqrt{\frac{3YI\,t_y}{M(0)}},$$

where $M(0)$ is the measured incremental base moment (Kaneko et al. (1998)).

In our generalized framework, this temporal fusion is implemented geometrically by intersecting the continuous feasible contact-point sets inferred at successive instants: $\mathcal{P}_{C,t} = \mathcal{P}_t \cap \mathcal{P}_{t-1}$, which may be extended to a sliding window $\mathcal{P}_{C,t} = \bigcap_{k=0}^{K-1} \mathcal{P}_{t-k}$ similar to the formulation reported by Sofla et al. (2024). Geometrically, this set-theoretic intersection is equivalent to the analytical closed-form solutions but extends naturally beyond the small-angle assumption, accommodating severe nonlinear bending and multimodal sensor fusion beyond observation of only bending moment.

In accordance with our propositions in Section 5.1, this geometric intersection collapses the continuous feasible curves into a tightly bounded subset or a unique point. Resolving this spatial intersection isolates a specific whisker shape α, which in turn yields a strictly finer partition of the augmented state space Q_{aug} for robot localization.

We apply this intersection strategy to estimate the contact point for the various virtual sensor models presented in Section 4.2. Fig. 8 illustrates the contact points estimated for these models under a linear base displacement of 1 mm along the y-axis, using the elastica2D model. The results demonstrate that intersecting the sets of possible contact points—either through temporal filtering or multi-modal fusion—collapses the multiplicity of hypotheses, strictly isolating the contact point.

Despite providing a robust initial estimate, this approach highlights the limitations of the contact strip and moment models in the large-angle deflection regime. As illustrated in Fig. 7, these models occupy lower tiers in the sensor hierarchy; lacking sufficient observation components to capture the nonlinear bending mechanics, their induced preimages remain too coarse to uniquely isolate the contact point during significant deformation. Consequently, accurate estimation in these regimes necessitates the finer partitions of the state space inherently provided by higher-tier, multi-modal sensing.

Furthermore, the proposed geometric intersection method is evaluated against the analytical approach presented by Kaneko et al. (1998). The comparative accuracy results, detailed in Table 1, were obtained using the physical whisker sensor depicted in Fig. 11b.

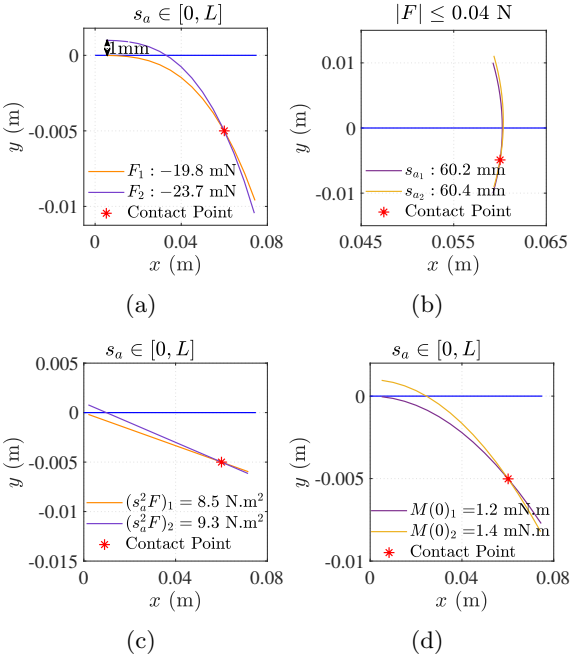


Fig. 8: Contact Point Determination for Simulated Virtual Sensors: The precise contact location is resolved through the spatial intersection of possible contact points using temporal filtering and a linear base displacement. (a) Load sensor. (b) Contact strip sensor. (c) End-slope sensor. (d) Moment sensor (small-angle case).

Outputs Passed to Localization:

Within the proposed localization pipeline, the isolated contact point p_t serves as the primary spatial constraint on the robot state. Concurrently, the inferred whisker shape $\hat{\sigma}_t$ and the end-slope $\phi_{a,t}$ provide the necessary angular constraints for boundary alignment. These geometric parameters—specifically the Cartesian coordinates (p_x, p_y), the contact tangent $\phi_{a,t}$, and their associated uncertainty bounds—facilitate the precise registration of the whisker shape against a known environment map. This registration process determines the pose preimage at each sensing instant, establishing the foundation for the sequential localization framework detailed in the subsequent section.

5.3 Robot State from Contact Geometry

Recall that the planar robot state is denoted by $q = (q_x, q_y, q_\theta) \in Q \subseteq \mathbb{R}^2 \times S^1$. At time t,

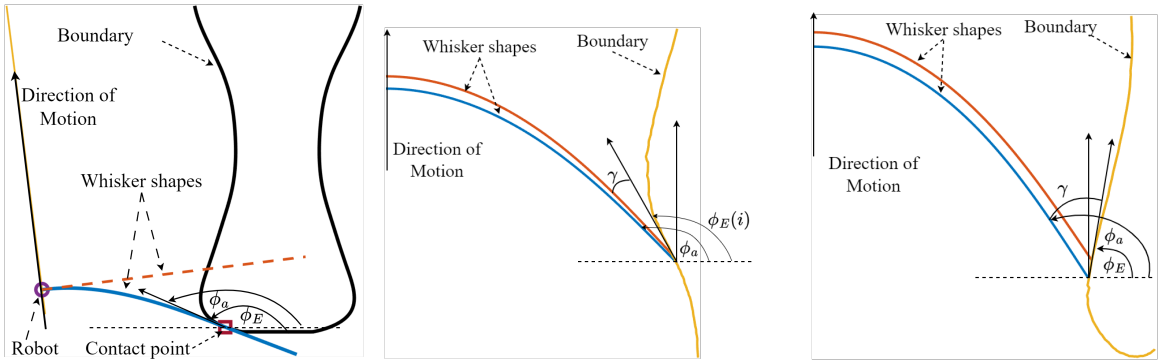


Fig. 9: Boundary alignment and whisker shape registration for preimage generation. (a) For contact along the whisker, geometric consistency is enforced by aligning the whisker slope at the contact point with the local boundary slope. (b) Evolution of the contact configuration as the whisker sweeps toward a concave boundary region, resulting in an increase in the apparent local boundary slope. (c) When the whisker sweeps away from a concave boundary region, resulting in a decrease in the apparent local boundary slope.

Table 1: Results of contact point estimation with a physical sensor. The sensor measures incremental moment $M(0)$ at the base with a base linear displacement of 1 mm. Results are compared with state-of-the-art analytical method presented in Kaneko et al. (1998); Solomon and Hartmann (2010).

p_x (mm)	$\hat{p}_x$ (mm)	$M(0)$ (mN · m)	$\hat{d}$ (Ours)	%ϵ	$\hat{d}$ (SOTA)	%ϵ
70	71.5	0.19	71.5	2.1	67.5	3.5
65	65.4	0.20	65.4	0.6	65.8	1.3
55	55.8	0.28	55.8	1.4	55.6	1.1
45	44.5	0.42	44.5	1.1	45.4	0.9
35	34.9	0.63	34.9	0.3	37.1	5.9

an observation z_t is processed using the filtering strategy from Section 5.1 to yield p_t, the uniquely estimated contact point in the whisker sensor reference frame. using the underlying cantilever beam mechanics, this isolated contact point maps deterministically to a uniquely deflected whisker shape $\hat{\sigma}_t$ (parameterized by α). By geometrically registering this specific shape against the known environment boundary, we construct the preimage $\mathbf{Q}_t \subset Q$, which encapsulates robot states consistent with the observation and whisker shape.

Whisker Shape Registration

Given the estimated contact point p_t, let $\phi_{a,t}$ denote the whisker tangent angle at the contact location, and let $\phi_{E,t}$ denote the tangent angle of the environment boundary at a hypothesized contact point in the known map. The resolved contact geometry $(\hat{\sigma}_t, p_t)$ determines whether the contact occurs along the whisker shaft or at the tip. For contact along the whisker, geometric consistency requires the whisker and boundary to have identical local tangents. This condition is enforced through the whisker–boundary alignment error:

$$\gamma_t = |\phi_{a,t} - \phi_{E,t}| \tag{16}$$

For geometrically consistent contact along the whisker, this alignment error should be close to zero as shown in Fig. 9a. In contrast, tip contact only requires positional coincidence and does not impose a tangency constraint; therefore, the alignment error is not enforced as a feasibility condition in that case as shown in Fig. 9b and Fig. 9c.

All feasible robot states are obtained by transforming the candidate whisker shape such that its contact point p_t coincides with a boundary point. For shaft contacts, an additional tangency constraint is imposed by aligning the whisker tangent at contact with the local boundary tangent. For tip contacts, only the positional constraint is enforced.

During physical interaction, as the whisker sweeps along the environment, the contact tangent angle evolves according to the local boundary geometry. When the contact point approaches a concave region, the contact tangent angle increases, whereas when the contact point moves away from a concave region, the contact tangent angle decreases.

By repeating this boundary alignment procedure across all discretized boundary points for the resolved contact geometry $(\hat{\sigma}_t, p_t)$, we obtain the set of observation-consistent feasible robot states (pose preimage), denoted by $\mathbf{Q}_t$, assuming the whisker shape is known.

5.4 Localization

The localization framework is formulated as a recursive contraction of the feasible robot states, via an iterative sense–move–intersect cycle. This process assumes a known incremental motion input between successive sensing instants. To preserve the structural integrity of the whisker sensor (for an example, length $L = 75\,\text{mm}$) during experimental validation and autonomous deployment, the workspace is partitioned into clearance-based safety zones. As illustrated in Fig. 10, these zones facilitate trajectory planning that maintains sufficient obstacle engagement while preventing mechanical overstress of the sensor.

It must be emphasized that presence of robot mounted with a whisker sensor within a contact-feasible region (yellow or orange zones) is a necessary, but not sufficient, condition for a valid sensor observation. Physical contact is contingent upon the whisker geometry and the robot state q being oriented such that the sensor touches the environment boundary. In this study, the whisker is mounted laterally, i.e., perpendicular to the robot's longitudinal axis rather than aligned with the forward heading direction. Consequently, for any robot heading, the whisker samples the environment along the lateral direction in the body-fixed frame and can therefore make contact only with boundaries located to the side of the robot, rather than with obstacles lying ahead.

As shown in Fig. 10, Trajectory 1 represents a degenerate case for localization: as the robot moves parallel to the boundary, the whisker shape remains invariant. Such stationary observations yield insufficient geometric constraints to refine

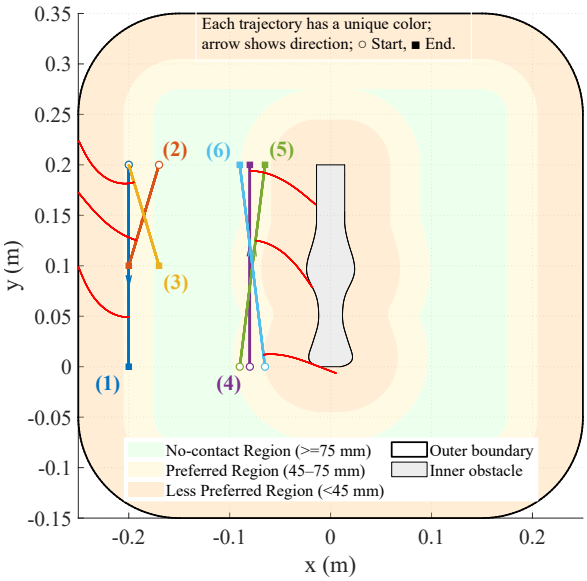


Fig. 10: Planar workspace and representative robot trajectories categorized by clearance-based safety zones. Background contours denote the minimum distance from the robot center to the environment boundaries when the length of whisker is L: green indicates a no-contact region (clearance $\geq 75\,\text{mm}$); yellow indicates the preferred contact-feasible region (45–75 mm); and orange indicates a region of significant deflection (clearance $< 45\,\text{mm}$). Circles and squares denote start and end positions, respectively, while arrows indicate the robot heading. Whisker shapes for different trajectories are shown in red.

the pose estimate. In contrast, the remaining trajectories traverse varying clearance contours, generating a sequence of distinct whisker shapes. These dynamic interactions provide the requisite geometric constraints to systematically resolve the robot state through the temporal intersection of successive preimages.

Forward Projection:

The transition from the current observation to the next sensing instant is realized through the set-valued action of the motion model on the feasible robot states $\mathbf{Q}_t$. Because the state estimate is represented as a set of admissible robot states, rather than as a single state, the motion update propagates every element of $\mathbf{Q}_t$ forward under the applied control input. The resulting predicted set is therefore

$$\hat{\mathbf{Q}}_{t+1} = \{\, f(q, u_t) \mid q \in \mathbf{Q}_t \,\}.$$

In the planar rigid-body setting, this propagation corresponds to composition with the incremental transform $T_{\text{local}} \in SE(2)$. Specifically, if a feasible state $q \in \mathbf{Q}_t$ is represented by the state transform $T(q)$, then its forward projected state is

$$T(q)' = T(q)\, T_{\text{local}}. \tag{17}$$

Hence, each element of $\hat{\mathbf{Q}}_{t+1}$ is obtained by forward projection of a feasible state in $\mathbf{Q}_t$ under the applied motion.

Bounded-Error State Estimation

The localization framework utilizes a recursive structure analogous to a Kalman filter, alternating between a prediction step (motion propagation) and a correction step (observation update). However, in contrast to probabilistic methods that propagate covariance matrices, this approach propagates and intersects feasible sets. In a deterministic context, given a new observation at time $t+1$, boundary alignment yields an observation-derived pose set $\mathbf{Q}_{t+1}^{\text{obs}}$. The corresponding observation update is then computed as the strict intersection:

$$\mathbf{Q}_{t+1} = \hat{\mathbf{Q}}_{t+1} \cap \mathbf{Q}_{t+1}^{\text{obs}}. \tag{18}$$

At the level of augmented states, temporal contraction is expressed as the set intersection of preimages within Q_{aug} when the shape of whisker is known:

$$\Delta_t = h^{-1}(z_t) \cap \Phi(\Delta_{t-1}), \tag{19}$$

where $h^{-1}(z_t)$ denotes the preimage induced by the current virtual sensor observation and $\Phi(\cdot)$ represents the forward propagation under a known incremental motion. Geometrically, each observation constrains the pair (q, α) to a subset of Q_{aug}; the iterative intersection of these subsets systematically contracts the feasible set.

However, deterministic intersections may become brittle—resulting in empty sets—when subjected to bounded sensing (observation) and motion errors. To ensure robustness, we adopt a possibilistic, set-valued observation model. In this formulation, the sensor mapping H accounts for noise such that:

$$H : Q \times \mathcal{A} \to \text{pow}(Z), \tag{20}$$

where $\mathcal{A} = [\alpha_{\min}, \alpha_{\max}]$ represents the parameter space, Z is the observation space, and $\text{pow}(\cdot)$ denotes the power set. Assuming a known bound on sensor observation noise $\varepsilon > 0$, the set-valued mapping is defined as:

$$\begin{aligned} H(q,\alpha) &= \{z \in Z \mid |h(q,\alpha) - z| \le \varepsilon\}, \\ H^{-1}(z) &= \{(q,\alpha) \mid z \in H(q,\alpha)\}. \end{aligned} \tag{21}$$

This formulation effectively expands the observation preimages from one-dimensional curves into robust patches or regions. The localization update is subsequently performed by intersecting the forward-projected regions with the newly defined possibilistic preimage, thereby ensuring stability against bounded noise while maintaining the integrity of the feasible pose set.

6 Experiments

This section presents the results of the experimental evaluation of the proposed whisker-based localization framework. Section 6.1 first describes the sensor design, fabrication, calibration and the experimental setup used for validation. Section 6.2 reports the simulation results, focusing on the effects of environmental symmetry and boundary curvature on the contraction of the robot's feasible state set. Finally, Section 6.3 presents the physical experimental results, including the comparison between deterministic and possibilistic update strategies and the resulting localization accuracy.

6.1 Sensor Design and Calibration

Hardware Architecture

The whisker sensor used in this study is designed to be modular and easy to reproduce. It is based on earlier designs reported by Lin et al. (2022); Kim et al. (2019); Routray et al. (2025). The current design uses a straight flexible Nitinol wire, as shown in the CAD model (Fig. 11a). The final prototype used in the experiments is shown in Fig. 11b.

The materials were chosen to improve the overall response of the sensor. The sensor base is 3D printed using Polylactic Acid (PLA), which has a density of $\rho = 1230\,\text{kg}\,\text{m}^{-3}$, a Young's modulus of $Y = 4.1\,\text{GPa}$, and a Poisson's ratio of $\nu = 0.35$.

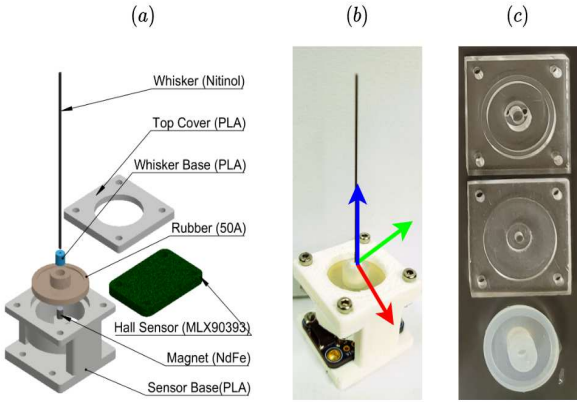


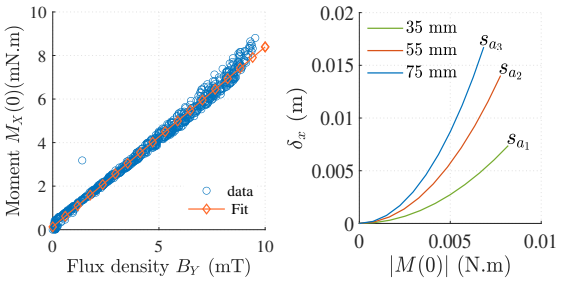
Fig. 11: Whisker sensor architecture: (a) CAD model illustrating structural components; (b) the fully fabricated prototype; (c) the Liquid Silicone Rubber (LSR) compliant element (CE) and the corresponding acrylic mold used for fabrication.

The compliant pivot mechanism allows the stiffness to be adjusted by changing its geometry, specifically its thickness and diameter. It is made from Liquid Silicone Rubber (LSR) with a Shore hardness of 50A. The LSR was prepared by mixing Part-A and Part-B in a 1:1 ratio by weight, then poured into a precise acrylic mold (Fig. 11c) and cured for 24 hours. The whisker (cantilever beam) is a thin Nitinol wire with an effective length of 75 mm and a diameter of 0.58 mm. The physical properties of the Nitinol wire, which determine the whisker shape under load, are a Young's modulus of $Y = 52\,\text{GPa}$, a density of $\rho = 6450\,\text{kg}\,\text{m}^{-3}$, and an area moment of inertia of $I = 5.555 \times 10^{-15}\,\text{m}^4$.

Transduction and Calibration

The whisker sensor deflection records a signal at the base recorded using an MLX90393 triaxial Hall-effect sensor. This sensor has 16-bit resolution and a configurable magnetic flux range of $\pm 5\,\text{mT}$ to $\pm 50\,\text{mT}$. The design is also compatible with other transducers, such as the TLE493D Hall sensor, which provides 12-bit resolution up to $\pm 160\,\text{mT}$. When the Nitinol wire makes contact with an obstacle,the Hall-effect sensor at the base converts the mechanical deflection into a readable magnetic flux density.

For the physical prototype, the magnetic flux density B is mapped to estimate the base bending moment $M(0)$ via calibration (Fig. 12a). While $M(0)$ reliably facilitates contact point estimation under small-angle assumptions, its accuracy is limited for large-angle deflections due to the non-injective nature of the $M(0) \rightarrow \delta_x$ mapping (Fig. 12b). However, if the sensing architecture allows for the direct observation of the contact arc-length s_a (e.g., via a contact-strip sensor: model 3), the complete set $\{F, s_a, \phi_a\}$ can be recovered deterministically. This direct observation of arc-length provides the full geometric information required to estimate the contact point p_t and whisker shape $\hat{\sigma}_t$ across all deflection regimes.

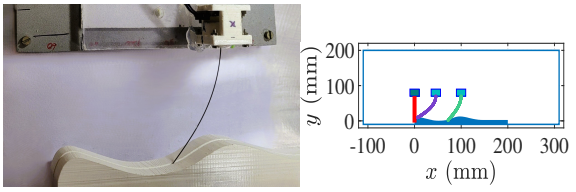


(a) (b)

Fig. 12: (a) Calibration mapping of flux density to base bending moment. (b) Mapping of base bending moment to horizontal deflection δ_x (refer to Fig. 1b).

Experimental Setup

The experimental setup for physical whisker sensor based localization uses a high-precision linear stage. The linear stage provides ground-truth position, enabling the evaluation of the recursive sense–move–intersect update cycle established in Section 5.4. Fig. 13 illustrates the experimental setup, in which the whisker sensor sweeps along a rigid obstacle boundary to resolve the robot's global state.



(a) (b)

Fig. 13: Experimental setup: (a) The whisker sensor (Fig. 11b) is mounted on a linear stage and brushes against an obstacle. (b) The estimated shape of the whisker sensor during contact.

6.2 Simulation Results

We tested the localization framework in a simulated environment where the contact geometry $(\hat{\sigma}_t, p_t)$ and the ground-truth pose $q_t^\star$ are known at each sensing step. This setup allows for a direct comparison between the estimated feasible set $\mathbf{Q}_t$ and the true robot pose.Fig. 14 illustrates the robot trajectory alongside all possible discretized robot states based on a single observation and the corresponding whisker shape. To simplify computations, the environment boundary is discretized to a 1 mm distance. Accordingly, the robot states are determined using the whisker shape registration method described in Section 5.3.

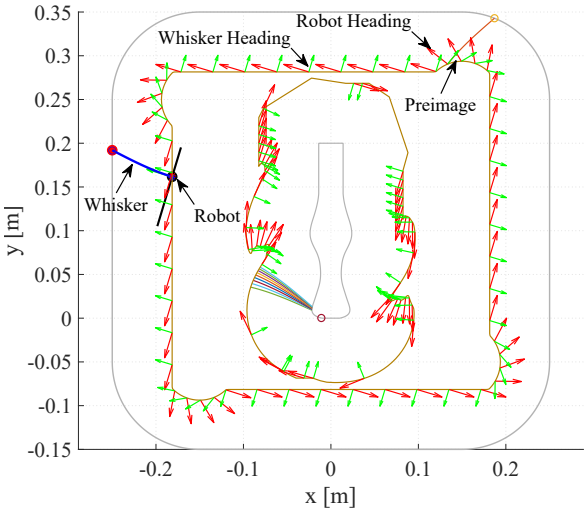


Fig. 14: The discretized preimage—derived from the discretization of the environment boundary—displays all feasible robot states, including orientation. The whisker maintains contact with the outer boundary while the robot follows trajectory type-2 (see Fig. 10).

Localization with Environmental Ambiguity

In environments with straight featureless boundaries and symmetric corners, localization is limited by the geometry of the map. As shown in Fig. 15a, the intersection of the forward projected set $\hat{\mathbf{Q}}_t$ with the observation-derived preimage $\mathbf{Q}_t^{\text{obs}}$ reduces the number of candidate poses. Since both the current preimage and the forward projected preimage are discrete, an exact spatial intersection may fail to capture valid states due to discretization artifacts—an issue not present in the continuous case. To make this intersection robust, we apply a 1 mm buffer when comparing the forward projected preimage with the new observation preimage. In particular, a state in the new observation preimage is retained if there exists a state in the forward projected preimage within a radius of 1 mm. Thus, the intersection is evaluated in a buffered sense rather than by exact coincidence of discrete samples. Even with this reduction, the process does not produce a unique solution after several sense–move–intersect cycles. In the continuous case, the resulting robot states are segments along the boundary. In the discrete case, this appears as elongated clusters of feasible robot states along the straight boundary segments. This happens because motion parallel to a featureless wall produces observation preimages that doesn't provide an observation to induce partition refinement.

This ambiguity is further compounded by environmental symmetry. Repeated corner shapes can yield identical preimages under certain environmental rotations and reflections. As a result, multiple distinct state hypotheses may remain consistent with the sensor readings over successive updates. As illustrated in Fig. 15b, the inclusion of orientation information partially mitigates this ambiguity. The valid states within the orientation-informed preimage are enclosed by dotted ellipses, indicating a significant reduction in the number of feasible discrete robot states. A unique state estimate requires preimages that break this symmetry further, such as those generated by contact with non-parallel boundaries or boundaries with unique local features (boundary with textures), as reported by Routray et al. (2022).

Localization via Non-Linear Boundaries

To address the ambiguity caused by straight and symmetric boundaries, we evaluated a completely different robot trajectory designed specifically to interact with non-linear boundary segments. Unlike straight walls, curved or irregular boundaries generate preimages that vary distinctly depending on the contact position, as illustrated in Fig. 16. When the whisker interacts with these non-linear features, the resulting preimages effectively break the translational symmetry typically found along straight segments.

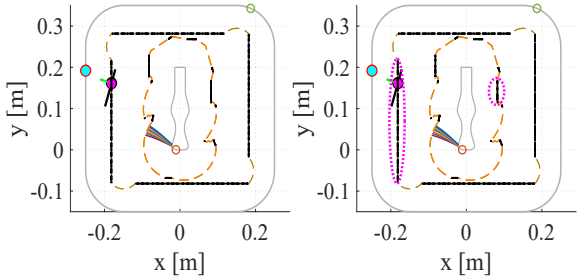


Fig. 15: (a) Candidate robot states resulting from the intersection of the forward projected set and the newly induced preimage. Straight boundaries and symmetric corners lead to elongated clusters of feasible states. (b) Refinement of the feasible set using orientation-informed preimages (highlighted by dotted ellipses), which partially reduce the rotational symmetry of the environment.

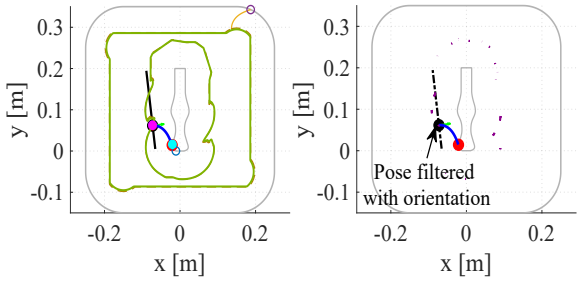


Fig. 16: (a) Feasible state set $\mathbf{Q}_t$ following contact with non-linear boundary segments. The geometric variation in the induced preimages reduces the number of disjoint state clusters compared to linear boundaries. (b) Faster localization through the intersection of orientation-informed preimages, resulting in the isolation of the ground-truth state.

Consequently, the intersection of these geometrically distinct preimages accelerate the contraction of the feasible state set, as shown in Fig. 16a and Fig. 16b. This rapid convergence yields a significantly smaller discrete state set compared to trajectories restricted to featureless boundaries. These results demonstrate that the environment boundary plays a critical role in whisker-based contact sensing, and that motion strategies can be purposefully designed to overcome the ambiguities associated with environmental symmetry.

Robot State Set Contraction

The reduction in state uncertainty is quantified by measuring the cardinality of the feasible set $\mathbf{Q}_t$ as successive preimages are intersected. As introduced previously, we apply a 1 mm spatial buffer during each intersection to account for discretization artifacts, ensuring that valid robot states are not inadvertently discarded over repeated sense–move–intersect cycles. Fig. 17 illustrates this convergence. The results demonstrate that trajectories allowing the whisker to sweep across diverse boundary geometries, particularly convex and concave segments, yield a higher rate of set contraction. These non-linear segments generate more informative preimages, which helps isolate the true robot state more rapidly.

In contrast, trajectories restricted to the outer boundary—which primarily consists of straight and symmetric segments—exhibit significantly slower convergence. In these regions, the induced preimages remain similar under translation, preventing the feasible set from shrinking to a singleton. However, incorporating orientation-informed preimages helps break this symmetry and accelerates the reduction of ambiguity, even in structurally symmetric environments.

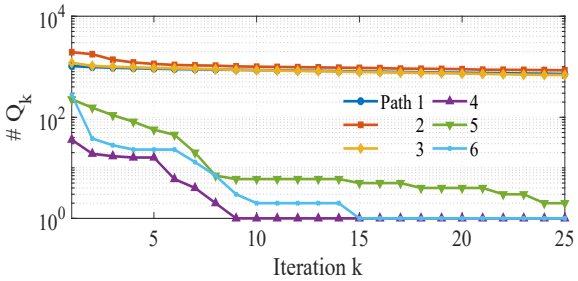


Fig. 17: Evolution of the feasible state set cardinality over successive iterations. The plot compares the contraction rates for trajectories that allow the whisker to sweep across boundaries with different curvatures and for trajectories constrained by environmental symmetry.

6.3 Physical Experimental Results

The localization using a physical whisker sensor follows the same method as discussed in simulation. At each discrete time t, the sensor reading is used to estimate the contact geometry, which is then used to construct the pose preimage $\mathbf{Q}_t^{\text{obs}}$

through boundary alignment. As in the simulation study, the feasible pose set is forward projected using the known incremental motion and then updated using either the deterministic rule in Eq.(18) or the possibilistic rule in Eq.(21) to contact the robot state set.

Tip-Contact Interpretation

While the localization algorithm can successfully process contact anywhere along the length of the whisker, the transition to tip contact represents a critical and highly advantageous phase. Within the set-theoretic framework, this specific transition is detected when the set of feasible contact points, $\mathcal{P}_C$, narrows down solely to the tip ($s = L$)—or becomes empty—yet the transducer continues to record a valid signal above the noise threshold.At this stage, the mapping $B \to M(0)$ and the associated geometric calculations become highly dependable because the contact distance is definitively fixed to the full length of the whisker ($s_a = L$). Because this geometric uncertainty is reduced, the system can more readily determine the required set of variables, $\{F, L, \phi_a\}$ based on the calibration and beam mechanics. Consequently, the robot states, $\mathbf{Q}_t^{\text{obs}}$, can be estimated. Ultimately, by recognizing this shift from contact along the whisker to tip contact, the algorithm can utilize the more stable geometry to rapidly narrow down the set of possible robot states.

Deterministic vs. Possibilistic Localization

Building on the simulation framework, the proposed approach was validated using the physical whisker sensor to evaluate recursive preimage updates under real-world conditions. Ground-truth displacement for error measurement (translation and orientation) was provided by a high-precision linear stage. To account for discretization artifacts during spatial intersections, we consistently applied the 1 mm buffer introduced in Section 6.2. The following results contrast the deterministic and possibilistic implementations, highlighting the fundamental trade-off between strict set precision and algorithmic robustness in the presence of physical noise.

The results of the deterministic intersection process are illustrated in Fig. 18a–b. Initially, a single physical sensor observation generates a widely distributed set of candidate robot states (blue scattered points). Over four iterations of the recursive sense–move–intersect cycle, the strict intersection of these preimages rapidly contracts the feasible set (red scattered points), effectively eliminating inconsistent state hypotheses. However, despite the inclusion of the 1 mm spatial buffer, the deterministic approach remains highly brittle in practice. Because it demands absolute geometric consistency, minor calibration inaccuracies or unmodeled sensor noise frequently overconstrain the system, rapidly driving the feasible state set to an empty set.

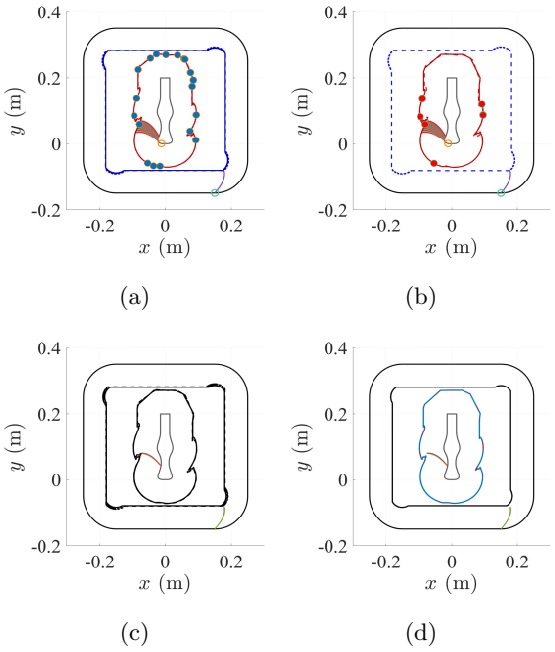


Fig. 18: Comparative analysis of physical localization strategies using the whisker sensor: (a–b) Deterministic Localization, showing the refinement of the feasible pose set (blue to red) after four iterations. (c–d) Possibilistic Localization, illustrating the enclosure of the robot pose within subsets (red) under bounded observation uncertainty.

Conversely, the possibilistic localization results (shown in Fig. 18c–d) demonstrate how relaxing the strict intersection requirement accommodates bounded observation uncertainty. Specifically, to account for unmodeled physical variations, we apply a 5% error margin to the physical sensor

observations during the conversion of magnetic flux density to bending moment. By evaluating the consistency of candidate states against these bounded error margins, the algorithm reliably maintains the true robot state within the computed subsets (red patches). While this possibilistic approach yields a geometrically larger final set of candidate states compared to the ideal deterministic case, it effectively prevents the abrupt emergence of an empty set caused by physical sensor inaccuracies. Ultimately, this ensures the continuous tracking and robustness required when localizing a robot using a physical whisker sensor.

6.4 Localization Error Analysis

To evaluate localization accuracy, the recorded ground-truth positions were synchronized with the corresponding sensor observations. Within the possibilistic framework, the localization error is calculated by measuring the spatial deviation between the known ground-truth pose and a representative estimate derived from the bounded feasible state set.During the physical trials, the sensor swept along concave boundaries that produce consistent variations in the observations. The summary performance data for these physical trials are detailed in Table 2, which reports the mean error (μ) and standard deviation (SD) across the full trajectory. The average localization error remained below 7.5 mm across the tested conditions.

Table 2: Average localization error for different whisker sweeps along the obstacle boundary.

Sweep ID	01	02	03	04	05
μ (mm)	2.79	6.20	3.60	5.50	7.30
SD (mm)	1.09	1.67	0.02	0.65	0.44

Experimental sweeps were conducted for various sweep IDs under similar conditions, as shown in Fig. 13. Each sweep ID corresponds to a specific, known starting location along the obstacle boundary from which the localization process initiates. During these trials, the motion model parameters (t_x, t_y) were varied, and the number of samples used to estimate the instantaneous boundary slope ϕ_{E_i} ranged from 2 to 5. The linear motion per step (t_x or t_y) was constrained to less than 1 mm, which is consistent with the spatial resolution of the discretized environment boundary.

7 Discussion

Preimage-Based Sensor Comparison

The proposed framework treats proprioceptive whisker sensing through the preimages induced by its observation models. Under this view, different measurable quantities correspond to distinct feasible sets within the combined robot-whisker state space. This perspective allows varying sensing modalities to be evaluated, compared, and formally ordered based on the state uncertainty they correspond to.

Consequently, the resulting virtual whisker hierarchy provides a unified representation for analyzing uncertainty across different sensor models, entirely decoupling the mathematical formulation from any specific hardware implementation.

Localization Results

The physical sensor based localization experiments provide a concrete validation of this framework within a planar setting. Because whisker observations are inherently non-injective—meaning multiple robot states can yield the exact same sensor reading—a single observation is insufficient for global localization. However, as demonstrated, recursive preimage intersection systematically reduces this pose ambiguity when combined with known incremental motion and a mapped environment. These results clearly illustrate how our theoretical formulation directly connects the underlying structure of the observation model to downstream state estimation performance.

Assumptions of the Formulation

The analysis in Section 3 relies on a few specific conditions. First, it assumes the system operates in a 2D (planar) environment with slow, steady movements (quasi-static) and that the whisker only makes contact at a single point. Second, it assumes the robot's incremental movements are known and that the whisker bends according to the large-deflection Euler-Bernoulli beam model. Finally, the sensor readings must consistently and

reliably map to the actual shape of the whisker so the system can calculate the geometry. While these assumptions are necessary to render the formulation mathematically tractable, they also set strict limits on where and how this model can be applied in the real world.

Limitations of the Current Formulation

Operating within these boundaries means that several physical effects fall outside the scope of the present formulation. Unmodeled phenomena such as out-of-plane deformation, torsional twisting, dynamic contact forces, boundary slip, and broader forms of mechanical model mismatch can degrade the consistency of the inferred preimages, potentially compromising the set intersections. Additionally, the current implementation relies on discrete approximations of both continuous state sets and map boundaries. As observed during the experiments, this discretization reduces spatial resolution and can introduce geometric artifacts, particularly near corners and other structurally sensitive regions of the environment.

8 Conclusion

This paper presented a preimage-based formulation for proprioceptive whisker sensing alongside a corresponding set-based framework for contact estimation and robot self-localization in known planar environments. By representing whisker sensor observations through their induced preimages and partitioning of augmented state-space, the approach makes it possible to explicitly account for the non-injective nature of whisker observations and to systematically reduce ambiguity through recursive set intersection combined with known incremental motion.

The proposed framework was evaluated in both experiment and simulation. Physical experiments with a low-cost Hall-effect whisker sensor demonstrated the feasibility of contact estimation and obstacle profile reconstruction. Furthermore, the framework effectively exploits the transition to tip contact, which definitively fixes the arc length and accelerates the contraction of the feasible robot states. The experimental trials—validated against a high-precision linear stage—enabled quantitative evaluation of localization accuracy across multiple sweeps and different trajectories in simulation.

Crucially, the physical implementations highlighted the inherent sensitivity of strict deterministic intersections to real-world observation noise. The results demonstrate that adopting a possibilistic approach, which accommodates bounded observation uncertainty, successfully prevents premature convergence to empty sets and ensures robust tracking. Finally, this work illustrates how preimage-based models can be utilized to analyze and formally order whisker sensor models based on the state uncertainty they induce, fundamentally linking purposeful sensor design to reliable downstream estimation and navigation tasks.

Declarations

Funding: This work was supported by a European Research Council Advanced Grant (ERC AdG, ILLUSIVE: Foundations of Perception Engineering, 101020977).
Conflict of interest: The authors declare no competing interests.

Author Contributions

Prasanna K. Routray: Investigation, sensor design, mathematical analysis, experiments, and original draft preparation.
Basak Sakcak: Conceptualization, mathematical analysis, and manuscript revision.
Steven M. LaValle: Conceptualization, intellectual guidance, and funding acquisition.
Manivannan M.: Conceptualization, research supervision.

All authors contributed to result interpretations and approved the final version for publication.

Acknowledgements

The authors gratefully acknowledge Prof. Mitra J. Hartmann for providing access to the *elastica2D* model, which was instrumental in this study.

Appendix A Cantilever at Large-Angle Deflection

The mechanics of the large-angle deflection (see Fig. 1b) regime are governed by the elastica model, where the beam geometry is no longer approximated by linear curvature. For a point force F applied at an arbitrary arc-length s_a, the deflected shape for $0 \leq s \leq s_a$ is given by the following elliptic integrals (see Beléndez et al. (2002)):

$$\begin{aligned} x(s) &= \sqrt{\frac{YI}{2F}} \int_0^{\phi(s)} \frac{\cos\phi}{\sqrt{\sin\phi_a - \sin\phi}}\, d\phi, \\ y(s) &= \sqrt{\frac{YI}{2F}} \int_0^{\phi(s)} \frac{\sin\phi}{\sqrt{\sin\phi_a - \sin\phi}}\, d\phi, \end{aligned} \tag{A1}$$

where $\phi_a = \phi(s_a)$ is the slope at the contact/load application point. If ϕ_a is unknown, it can be numerically estimated from the arc-length using

$$s_a = \sqrt{\frac{YI}{2F}} \int_0^{\phi_a} \frac{1}{\sqrt{\sin\phi_a - \sin\phi}}\, d\phi. \tag{A2}$$

For the unloaded section $s_a < s \leq L$, the beam maintains constant slope ϕ_a, and the shape is described by

$$\begin{aligned} x(s) &= x(s_a) + (s - s_a)\cos\phi_a, \\ y(s) &= y(s_a) + (s - s_a)\sin\phi_a. \end{aligned} \tag{A3}$$

The point $(p_x, p_y) = \big(x(s_a), y(s_a)\big)$ corresponds to the location of contact. Since the integrals involve elliptic functions, closed-form solutions are unavailable, and numerical approximation is required.

In small-angle cases, the horizontal displacement is negligible ($\delta_x \to 0$), and the vertical deflection reaches its peak at the free end ($s = L$). However, for the general large-deflection case, the bending moment generated at any position $s < s_a$ from a load F applied at $s = s_a$ is given by

$$M(s) = F[x(s_a) - x(s)] = F \int_s^{s_a} \cos\phi\, ds, \tag{A4}$$

where $\cos\phi = \frac{dx}{ds}$. At the base ($s = 0$), this simplifies to $M(0) = Fx(s_a)$, and for a load at the tip, $M(0) = Fx(L)$. For $s > s_a$, $M(s) = 0$, since the load is applied upstream.

References

Ahn, S., Kim, D.: Radial distance estimation with tapered whisker sensors. Sensors **17**(7), 1659 (2017) https://doi.org/10.3390/s17071659

Bilevich, M.M., LaValle, S.M., Halperin, D.: Sensor localization by few distance measurements via the intersection of implicit manifolds. In: 2023 IEEE International Conference on Robotics and Automation (ICRA), pp. 1912–1918 (2023). https://doi.org/10.1109/ICRA48891.2023.10160553 . IEEE

Beléndez, T., Neipp, C., Beléndez, A.: Large and small deflections of a cantilever beam. European journal of physics **23**(3), 371 (2002) https://doi.org/10.1088/0143-0807/23/3/317

Boubenec, Y., Shulz, D.E., Debrégeas, G.: Whisker encoding of mechanical events during active tactile exploration. Frontiers in behavioral neuroscience **6**, 74 (2012) https://doi.org/10.3389/fnbeh.2012.00074

Birdwell, J.A., Solomon, J.H., Thajchayapong, M., Taylor, M.A., Cheely, M., Towal, R.B., Conradt, J., Hartmann, M.J.: Biomechanical models for radial distance determination by the rat vibrissal system. Journal of neurophysiology **98**(4), 2439–2455 (2007) https://doi.org/10.1152/jn.00707.2006

Chen, R., Xu, J., Zhang, S.: Comparative study on 3d optical sensors for short range applications. Optics and lasers in engineering **149**, 106763 (2022) https://doi.org/10.1016/j.optlaseng.2021.106763

Deer, W., Pounds, P.E.: Lightweight whiskers for contact, pre-contact, and fluid velocity sensing. IEEE Robotics and Automation Letters **4**(2), 1978–1984 (2019) https://doi.org/10.1109/LRA.2019.2899215

Emnett, H., Graff, M., Hartmann, M.: A novel whisker sensor used for 3d contact point determination and contour extraction. In: Proceedings of Robotics: Science and Systems, vol.

14. Robotics: Science and Systems, ??? (2018). https://doi.org/10.15607/RSS.2018.XIV.059

Fox, C., Evans, M., Pearson, M., Prescott, T.: Tactile slam with a biomimetic whiskered robot. In: 2012 IEEE International Conference on Robotics and Automation, pp. 4925–4930 (2012). https://doi.org/10.1109/ICRA.2012.6224813 . IEEE

Gazzola, M., Dudte, L.H., McCormick, A.G., Mahadevan, L.: Forward and inverse problems in the mechanics of soft filaments. Royal Society open science **5**(6), 171628 (2018) https://doi.org/10.1098/rsos.171628

Guyonneau, R., Lagrange, S., Hardouin, L., Lucidarme, P.: Guaranteed interval analysis localization for mobile robots. Advanced Robotics **28**(16), 1067–1077 (2014) https://doi.org/10.1080/01691864.2014.908742

Huet, L.A., Emnett, H.M., Hartmann, M.J.: Demonstration of three-dimensional contact point determination and contour reconstruction during active whisking behavior of an awake rat. PLoS computational biology **18**(9), 1007763 (2022) https://doi.org/10.1371/journal.pcbi.1007763

Huet, L.A., Rudnicki, J.W., Hartmann, M.J.: Tactile sensing with whiskers of various shapes: Determining the three-dimensional location of object contact based on mechanical signals at the whisker base. Soft robotics **4**(2), 88–102 (2017) https://doi.org/10.1089/soro.2016.0028

Jaulin, L.: A nonlinear set membership approach for the localization and map building of underwater robots. IEEE Transactions on Robotics **25**(1), 88–98 (2009) https://doi.org/10.1109/TRO.2008.2010358

Kaneko, M., Kanayama, N., Tsuji, T.: Active antenna for contact sensing. IEEE Transactions on robotics and automation **14**(2), 278–291 (1998) https://doi.org/10.1109/70.681246

Kim, D., Möller, R.: Passive sensing and active sensing of a biomimetic whisker. In: International Conference on the Simulation and Synthesis of Living Systems. Bloomington: Indiana University Press, pp. 127–131 (2006)

Kim, D., Möller, R.: Biomimetic whiskers for shape recognition. Robotics and Autonomous Systems **55**(3), 229–243 (2007) https://doi.org/10.1016/j.robot.2006.08.001

Kim, S., Velez, C., Patel, D.K., Bergbreiter, S.: A magnetically transduced whisker for angular displacement and moment sensing. In: 2019 IEEE/RSJ International Conference on Intelligent Robots and Systems (IROS), pp. 665–671 (2019). https://doi.org/10.1109/IROS40897.2019.8968518 . IEEE

LaValle, S.M., *et al.*: Sensing and filtering: A fresh perspective based on preimages and information spaces. Foundations and Trends® in Robotics **1**(4), 253–372 (2012) https://doi.org/10.1561/2300000004

Lepora, N.F., Pearson, M., Cramphorn, L.: Tacwhiskers: Biomimetic optical tactile whiskered robots. In: 2018 IEEE/RSJ International Conference on Intelligent Robots and Systems (IROS), pp. 7628–7634 (2018). https://doi.org/10.1109/IROS.2018.8593653 . IEEE

Lin, M.A., Reyes, E., Bohg, J., Cutkosky, M.R.: Whisker-inspired tactile sensing for contact localization on robot manipulators. In: 2022 IEEE/RSJ International Conference on Intelligent Robots and Systems (IROS), pp. 7817–7824 (2022). https://doi.org/10.1109/IROS47612.2022.9982122 . IEEE

Mitchinson, B., Martin, C.J., Grant, R.A., Prescott, T.J.: Feedback control in active sensing: rat exploratory whisking is modulated by environmental contact. Proceedings of the Royal Society B: Biological Sciences **274**(1613), 1035–1041 (2007) https://doi.org/10.1098/rspb.2006.0347

Pearson, M.J., Mitchinson, B., Sullivan, J.C., Pipe, A.G., Prescott, T.J.: Biomimetic vibrissal sensing for robots. Philosophical Transactions of the Royal Society B: Biological Sciences **366**(1581), 3085–3096 (2011) https://doi.org/10.1098/rstb.2011.0164

Pearson, M.J., Pipe, A.G., Melhuish, C., Mitchinson, B., Prescott, T.J.: Whiskerbot: a robotic active touch system modeled on the rat whisker sensory system. Adaptive Behavior **15**(3), 223–240 (2007) https://doi.org/10.1177/1059712307082089

Prescott, T.J., Pearson, M.J., Mitchinson, B., Sullivan, J.C.W., Pipe, A.G.: Whisking with robots. IEEE robotics & automation magazine **16**(3), 42–50 (2009) https://doi.org/10.1109/MRA.2009.933624

Peternell, M., Steiner, T.: Minkowski sum boundary surfaces of 3d-objects. Graphical Models **69**(3-4), 180–190 (2007) https://doi.org/10.1016/j.gmod.2007.01.001

Quist, B.W., Hartmann, M.J.: Mechanical signals at the base of a rat vibrissa: the effect of intrinsic vibrissa curvature and implications for tactile exploration. Journal of neurophysiology **107**(9), 2298–2312 (2012) https://doi.org/10.1152/jn.00372.2011

Routray, P.K., Kanade, A.S., Tiwari, K., Pounds, P., Muniyandi, M.: Towards multidimensional textural perception and classification through whisker. In: 2022 IEEE International Symposium on Robotic and Sensors Environments (ROSE), pp. 1–7 (2022). https://doi.org/10.1109/ROSE56499.2022.9977409 . IEEE

Routray, P.K., Subudhi, D., Pounds, P., *et al.*: Whisker-like sensors: Effective design. In: 2025 13th International Conference on Control, Mechatronics and Automation (ICCMA), pp. 435–440 (2025). https://doi.org/10.1109/ICCMA67641.2025.11369557 . IEEE

Starostin, E., Goss, V., Heijden, G.: Whisker sensing by force and moment measurements at the whisker base. Soft Robotics **10**(2), 326–335 (2023) https://doi.org/10.1089/soro.2021.0085

Solomon, J.H., Hartmann, M.J.Z.: Extracting object contours with the sweep of a robotic whisker using torque information. The International Journal of Robotics Research **29**(9), 1233–1245 (2010) https://doi.org/10.1177/0278364908104468

Solomon, J.H., Hartmann, M.J.: Radial distance determination in the rat vibrissal system and the effects of weber's law. Philosophical Transactions of the Royal Society B: Biological Sciences **366**(1581), 3049–3057 (2011) https://doi.org/10.1098/rstb.2011.0166

Struckmeier, O., Tiwari, K., Salman, M., Pearson, M.J., Kyrki, V.: Vita-slam: A bio-inspired visuo-tactile slam for navigation while interacting with aliased environments, 97–103 (2019) https://doi.org/10.1109/CBS46900.2019.9114526 . IEEE

Sofla, M.S., Vayakkattil, S., Calisti, M.: Haptic localization with a soft whisker from moment readings at the base. Soft Robotics **11**(4), 539–549 (2024) https://doi.org/10.1089/soro.2023.0098

Tiwari, K., Sakcak, B., Routray, P., Manivannan, M., LaValle, S.M.: Visibility-inspired models of touch sensors for navigation. In: 2022 IEEE/RSJ International Conference on Intelligent Robots and Systems (IROS), pp. 13151–13158 (2022). https://doi.org/10.1109/IROS47612.2022.9981084 . IEEE

Takei, K., Yu, Z., Zheng, M., Ota, H., Takahashi, T., Javey, A.: Highly sensitive electronic whiskers based on patterned carbon nanotube and silver nanoparticle composite films. Proceedings of the National Academy of Sciences **111**(5), 1703–1707 (2014) https://doi.org/10.1073/pnas.131792011

Wang, S., Liu, J., Liu, B., Wang, H., Si, J., Xu, P., Xu, M.: Potential applications of whisker sensors in marine science and engineering: A review. Journal of Marine Science and Engineering **11**(11), 2108 (2023) https://doi.org/10.3390/jmse11112108

Yu, Z., Childs, P.R., Ge, Y., Nanayakkara, T.: Whisker sensor for robot environments perception: a review. IEEE Sensors Journal **24**(18), 28504–28521 (2024) https://doi.org/10.1109/JSEN.2024.3429373